

Wide Field CO Mapping in the Region of IRAS 19312+1950

Jun-ichi Nakashima¹, Dmitry A. Ladeyschikov², Andrej M. Sobolev²,
Yong Zhang^{3,4}, Chih-Hao Hsia^{3,4,5}, Bosco H. K. Yung⁶

ABSTRACT

We report the results of a wide field CO mapping in the region of IRAS 19312+1950. This IRAS object exhibits SiO/H₂O/OH maser emission, and is embedded in a chemically-rich molecular component, of which the origin is still unknown. In order to reveal the entire structure and gas mass of the surrounding molecular component for the first time, we have mapped a wide region around IRAS 19312+1950 in the ¹²CO $J = 1-0$, ¹³CO $J = 1-0$ and C¹⁸O $J = 1-0$ lines using the Nobeyama 45m telescope. In conjunction with the archival CO maps, we investigated a region with a size up to 20' × 20' around this IRAS object. We calculated CO gas mass assuming the LTE condition, a stellar velocity against to the interstellar medium assuming an analytic model of a bow shock, and absolute luminosity using the latest archival data and trigonometric parallax distance. The derived gas-mass (225 M_⊙ – 478 M_⊙) of the molecular component and the relatively large luminosity (2.63 × 10⁴ L_⊙) suggest that the central SiO/H₂O/OH maser source seems to be a red supergiant (RSG) rather than an asymptotic giant branch (AGB) star or post-AGB star.

¹Department of Astronomy and Geodesy, Ural Federal University,
Lenin Avenue 51, 620000, Ekaterinburg, Russia
Email(JN): nakashima.junichi@gmail.com

²Astronomical Observatory, Ural Federal University,
Lenin Avenue 51, 620000, Ekaterinburg, Russia

³Department of Physics, University of Hong Kong, Pokfulam Road, Hong Kong, China

⁴Laboratory for Space Research, Faculty of Science, The University of Hong Kong, Pokfulam Road, Hong Kong, China

⁵Space Science Institute, Macau University of Science and Technology, Avenida Wai Long, Taipa, Macau, China

⁶N. Copernicus Astronomical Center, Rabiańska 8, 87-100 Toruń, Poland

Subject headings: maser — stars: chemically peculiar — stars: individual (IRAS 19312+1950)
 — stars: jets — stars: late-type

1. Introduction

An isolated mid-infrared source, IRAS 19312+1950 (I19312, hereafter) exhibits SiO, H₂O and OH masers (Nakashima & Deguchi 2000, 2007; Nakashima et al. 2011), and the properties of the masers of this IRAS object are quite reminiscent of a mass-losing evolved star, such as asymptotic giant branch (AGB) stars, a post-AGB stars, and red supergiants (RSGs) (Nakashima et al. 2011). For example, exhibiting SiO maser emission is a typical characteristic of AGB stars and RSGs (Genzel et al. 1980; Jewell et al. 1984; Barvainis & Clemens 1984; Nakashima et al. 2000; Imai et al. 2002b; Deguchi et al. 2004; Nakashima & Deguchi 2006; Deguchi et al. 2010; Fok et al. 2012), a bipolar molecular jet traced in the H₂O maser line (Nakashima et al. 2011) is quite similar to that found in oxygen-rich AGB/post-AGB stars (Imai et al. 2002a; Yung et al. 2011), and the intensity ratio of the OH maser satellite line to the main lines (> 1 ; Nakashima et al. 2011) is consistent with that of mass-losing evolved stars with a cold dust envelope (Habing 1996; Yung et al. 2013, 2014). Infrared properties of I19312 are also consistent with those of mass-losing evolved stars. For example, the mass-loss rate obtained by fitting dust radiative transfer models supports the AGB star status (Murakawa et al. 2007), and the near-infrared morphology is reminiscent of that of post-AGB stars and proto-planetary nebulae (PPNe; Deguchi et al. 2004; Murakawa et al. 2007). In addition, Cooper et al. (2013) classified I19312 as an M-type supergiant, since the near-infrared spectrum exhibits continuum emission that peaks in the middle of the 1.5 μm –2.5 μm region as well as showing molecular absorption lines owing to their cool atmospheres and have strong H₂O absorption. Lumsden et al. (2013) similarly classified I19312 as a PPN, based on the properties of infrared spectra and images.

At the same time, however, some other observational characteristics of I19312 cannot be explained in the standard scheme of the stellar evolution in its late stage. For example, the gas-mass estimated from a single-dish CO radio observation is $10 M_{\odot} - 15 M_{\odot}$ (Nakashima et al. 2004; Nakashima & Deguchi 2005); such a large gas-mass is hardly explained as materials expelled from an AGB/post-AGB star (we give a new estimation of the gas mass in the present study; see, Section 4.1). Even if we assume an RSG with a larger initial-mass, the interpretation is not straightforward, because a rich-set of molecular species have been detected toward I19312 (Deguchi et al. 2004); it is not typical for RSGs. So far, more than a dozen of molecular species have been detected, including both carbon- and

oxygen-bearing molecules (Deguchi et al. 2004); the complex chemistry including carbon-bearing molecules seems to be unusual for mass-losing evolved stars exhibiting SiO, H₂O and OH masers, because those molecules of masers are usually found only in oxygen-rich chemistry. The intensity peak velocities of the radio molecular lines of carbon-bearing molecules almost exactly corresponds to the systemic velocity obtained from maser observations (Deguchi et al. 2004; Nakashima et al. 2011). Interestingly, the detected molecules include CH₃OH (Deguchi et al. 2004; Nakashima et al. 2015), which has not been detected so far in any other evolved stars (see, e.g., Kawaguchi et al. 1995; Charnley & Latter 1997; Cernicharo et al. 2000; He et al. 2008; Gomez et al. 2014). Furthermore, Class I methanol lines have been detected toward I19312 recently (Nakashima et al. 2015); the authors suggested that Class I methanol maser emission is emitted from an interaction region between the outflow of an RSG and ambient molecular components.

Although a possibility of a young stellar object (YSO), which somehow exhibits SiO, H₂O and OH masers, has been considered in the past (see, e.g., Nakashima et al. 2011), the characteristics of I19312 are clearly different from such YSOs embedded in molecular clouds. For instance, I19312 shows an isolated point-like feature in mid-infrared images (see, e.g., Nakashima et al. 2011), while all YSOs with SiO masers are deeply embedded in its natal clouds and therefore the background of such YSOs is generally quite bright at mid-infrared wavelengths (e.g., Ori IRc 2, W51 IRs 2, and Sgr B2 MD5; Hasegawa et al. 1986); this is not the case for I19312. We would also note that we do not see any enhancement of the number density of stars in optical/near-infrared images (i.e., DSS, 2MASS, and UKDISS) around I19312. For these reasons, I19312 most likely cannot be explained as a YSO or a star at pre-main-sequence stages¹.

We note that some groups working on massive YSOs have paid their attention on I19312, although no groups have provided a strong evidence for classifying I19312 as a YSO (three studies mentioned below picked out I19312 basically due only to a large flux densities in submm/mm continuum emission). Wienen et al. (2012) have surveyed NH₃ emission toward a flux-limited sample of submm clumps detected by the APEX Telescope Large Area Survey: the GALaxy (ATLASGAL), which is an unbiased continuum survey of the inner Galactic disk at 870 μ m. I19312 was included in their target list, and the NH₃ (1, 1) and (2, 2) lines were detected as Deguchi et al. (2004) already reported the detections of the same lines. The obtained rotational temperature (14.22 K) was consistent with that obtained in

¹We also note that a recent result of a near-infrared high-dispersion spectroscopy suggests that the ¹³C abundance is significantly enhanced compared to the ¹²C abundance toward the direction of the central star, and the ¹³C/¹²C abundance ratio is far beyond the range of star forming regions (Parfenov, S. in private communications).

Deguchi et al. (2004) within uncertainty (the value obtained by Deguchi et al. was 19 K). Csengeri et al. (2014) listed I19312 as one of the compact submm continuum sources that were identified in the ATLASGAL project. The measured source size was $33'' \times 28''$ with a position angle of 121° : the position angle is consistent with that of the molecular jet (108° – 130° ; Nakashima & Deguchi 2005; Nakashima et al. 2011). Shirley et al. (2013) searched the HCO^+ 3–2 and N_2H^+ 3–2 lines toward bright 1.1 mm continuum sources, which were found by the Bolocam Galactic Plane Survey (BGPS; Aguirre et al. 2011). Both lines were detected toward I19312, and this was the first detections of these lines.

So far, two hypotheses have been mainly considered for explaining I19312 (see, e.g., Nakashima et al. 2011): (1) a red nova formed by the merger of two main sequence stars (or two stars going to main sequence) and (2) a mass-losing evolved star, such as a post-AGB star or RSG, embedded in a small, isolated molecular cloud. However, both of two hypotheses have not been fully examined yet. One of the important viewpoints for considering the origin of I19312 is to see how the molecular gas of I19312 distributes and moves, particularly, in the outermost region of the nebulosity. The real extent and total mass of the molecular gas could be an important clue to distinguish the above two possibilities, because in the case (1) the total gas-mass cannot go beyond the total mass of merging stars (if we assume that additional gas does not flow into the merging system), while in the case (2) the total gas-mass can be much larger than the case (1). Through mapping observations in several molecular rotational lines (Nakashima & Deguchi 2004, 2005), we revealed that the central part of the nebulosity (within $15''$ – $20''$ from the central star) involves a spherically expanding component and a molecular bipolar outflow, while the behavior of the outermost nebulosity is still unknown. Although in the past we made two mapping observations with the Berkeley-Illinois-Maryland (BIMA) array and the Nobeyama Radio Observatory (NRO) 45 m telescope (Nakashima et al. 2004; Nakashima & Deguchi 2005) in the CO rotational lines, those observations were not sufficient enough to reveal the entire distribution of the molecular component of I19312, because the BIMA observation resolved out the outermost nebulosity (the largest spatial frequency covered by the BIMA observation was roughly $15''$ – $20''$), and also because the mapping region of the NRO single-dish observation was too small ($60'' \times 60''$).

Thus, in order to reveal the entire structure of the molecular component of I19312, we made a wide field CO mapping in a region around I19312 using the 25-BEam Array Receiver System (BEARS) mounted on the NRO 45m telescope. We also investigated a wide field ^{13}CO $J = 1-0$ line image of the Boston University-Five College Radio Astronomy Observatory (FCRAO) Galactic Ring Survey (GRS) (Jackson et al. 2006). In conjunction with both the new observation and archival data, we studied a region with a size up to $20' \times 20'$.

2. Observations and Data Reduction

The CO mapping observations in the region of I19312 were made in the period from 2013 May 23 – Jun 2 using the NRO 45 m telescope (project number: CG122002). In total, 33 hours of the observing time were assigned in 11 days (3 hours per day), and roughly 21 hours out of the assigned 33 hours were usable for the observation; the remaining time were lost due to either mechanical problems or bad weather conditions. We observed three CO isotope lines: i.e., $^{12}\text{CO } J = 1-0$, $^{13}\text{CO } J = 1-0$ and $\text{C}^{18}\text{O } J = 1-0$. The rest frequencies used in the analysis were taken from Lovas (1992, the values are given in Table 1). We used BEARS, which is a double-side band (DSB) superconductor-insulator-superconductor (SIS) heterodyne receiver array developed for the NRO 45 m telescope (Sunada et al. 2000). BEARS consists of 5×5 arrays with a fixed grid spacing of $41.1''$ (Yamaguchi et al. 2000). The spectroscopic data were recorded by digital autocorrelators with a bandwidth of 512 MHz, 1024 frequency channels, and a frequency resolution of 500 kHz (Sorai et al. 2000). The observed CO lines were placed at the center of the 512 MHz spectral window. The system temperature was ranged from 310 K to 550 K, depending on the observing frequency, weather conditions and the elevation of the telescope. The pointing accuracy was checked at the beginning and in the middle of each 3-hours observing session by observing the SiO $v = 1$ and 2, $J = 1-0$ lines of an AGB star V1111 Oph with the High-Electron-Mobility Transistor (HEMT) receiver H40; the pointing accuracy was typically within $1''-2''$. We adopted the chopper-wheel method, switching between a room-temperature load and the sky, for primary intensity calibrations. This corrects for atmospheric attenuation and antenna ohmic losses, and converts the intensity scale to the antenna temperature in DSB [T_{A}^* (DSB)]. The beam size, main beam efficiency and aperture efficiency of the telescope were $14.7''-16.0''$, 44%–49% and 30%–36%, respectively at 112 GHz (Note: BEARS consists of 25 arrays, and therefore the measurements of the beam size, main beam efficiency and aperture efficiency slightly vary from array to array; we used an averaged value in our analysis).

We mapped a $500'' \times 500''$ square region in the $^{12}\text{CO } J = 1-0$, $^{13}\text{CO } J = 1-0$ lines and in a $250'' \times 250''$ square region in the $\text{C}^{18}\text{O } J = 1-0$ line, using the on-the-fly (OTF) mapping technique (Sawada et al. 2008). The regions were centered at the 2MASS position of I19312 (19h 33m 24.249s, $+19^\circ 56' 55.65''$, J2000.0), and the sides of the squares were set along the directions of the right ascension (X-direction) and declination (Y-direction). We scanned the regions along the X- and Y-directions several times in turn, and the maps in the two scan-directions were merged using the Basket-Weave technique (Emerson & Graeve 1988). Scan numbers in each direction, rms. noises achieved, velocity coverages, velocity resolutions are summarized in Table 1. The scan speed applied was $30'' \text{ s}^{-1}$ throughout all observations.

In order to reduce the OTF data, we used the software package NOSTAR, which was

developed for handling BEARS data by NRO. We followed a standard reduction procedure instructed by NRO²; the standard procedure includes splitting spectra of each spectrometer, scaling the intensity, subtracting a baseline by fitting a low-order polynomial, flagging bad channels, applying the Basket-Weave technique, and creating FITS cubes. We applied the Bessel-Gaussian function to convolve the maps, using a grid spacing of 10". The image processing and analysis of the reduced FITS cubes were made using the software package Miriad (Sault et al. 1995).

In addition to the NRO data, we also used archival data of the Boston University-FCRAO Galactic Ring Survey (GRS). GRS is a molecular line survey of the inner Galaxy using the SEQUOIA multi-pixel array receiver on the FCRAO 14 m telescope in the ¹³CO $J = 1-0$ line (Jackson et al. 2006). The sensitivity, spectral resolution, angular resolution and sampling spacing of GRS are < 0.4 K, 0.2 km s^{-1} , $46''$ and $22''$, respectively. The location of I19312 is included in the two data cubes in the GRS archive³ (the file names of the used data in the archive are grs-55-cube.fits and grs-56-cube.fits). The image processing and analysis of the GRS data were made using the software package Miriad.

3. Results

In Figures 1 and 2, we present the velocity-channel maps of the BEARS observations in the ¹³CO $J = 1-0$ and ¹²CO $J = 1-0$ lines. Although we observed the C¹⁸O $J = 1-0$ line as well, the velocity-channel map of this line is omitted due to the low signal-to-noise ratio. In Figures 1 and 2, we can clearly see the isolated CO emission of I19312 at the mapping center (see, 34.5 km^{-1} – 38.5 km^{-1} in Figure 1 and 35.5 km^{-1} – 39.5 km^{-1} in Figure 2). In the present observation, we revealed the entire structure of the CO emission of the molecular component of I19312 for the first time. As shown in the BIMA observation (Nakashima & Deguchi 2005), the CO emission of I19312 shows a velocity gradient in the north-west to south-east direction (see, the lower panel of Figure 3). The velocity gradient is also confirmed in Figure 1 (see, 34.5 km^{-1} – 38.5 km^{-1}), while in Figure 2, the gradient is not very obvious due to the low signal-to-noise ratio of the ¹²CO $J = 1-0$ line and due also to the effect of self absorption (see, Nakashima & Deguchi 2005). In the upper panel of Figure 3, we show the velocity-integrated intensity (zero-moment) BEARS map of the ¹³CO $J = 1-0$ line in the vicinity of I19312; the contour map is superimposed on the UKIDSS J , H , K -band composite color image. Comparing between the upper and lower panels in Figure 3,

²see, <http://www.nro.nao.ac.jp/~nro45mrt/html/obs/otf/index-e.html>

³see, <http://grunt.bu.edu/grs-stitch/download-all.php>

it is evident that the angular-size of the emission region seen in the BEARS map is roughly twice larger than that seen in the BIMA map; this difference of the emission region suggests that the non-negligible amount of the flux was resolved out in the BIMA observation due to interferometry (Nakashima & Deguchi 2005). The angular-size of the emission region seen in the BEARS map is roughly $90''$ in the north-south direction and $120''$ in the east-west direction; this corresponds to 5.1×10^{18} cm and 6.8×10^{18} cm, respectively, at the distance of 3.8 kpc (Imai et al. 2011).

In Figure 3, we see that the intensity peak of the $^{13}\text{CO } J = 1-0$ line is shifted roughly $10''$ from that of the near-infrared emission in the north-west direction. This is due to the velocity gradient, which was already confirmed in the BIMA observation (Nakashima & Deguchi 2005). Since the intensity of the blue-shifted component is slightly larger than that of the red-shifted component, the intensity peak of the zero-moment emission is shifted to the north-west direction, in which the flux of the blue-shifted component is dominant.

The upper panel of Figure 4 shows the spatially integrated BEARS spectra of I19312 in the $^{13}\text{CO } J = 1-0$, $^{12}\text{CO } J = 1-0$ and $\text{C}^{18}\text{O } J = 1-0$ lines. The area of the integration is a circle with a diameter of $25''$, which is centered at the 2MASS position of I19312. The intensity peak velocity of the $^{13}\text{CO } J = 1-0$ of I19312 (at $\sim 35 \text{ km s}^{-1}$) is consistent with the intensity peak velocity of other molecular lines (roughly $35 \text{ km s}^{-1} - 36 \text{ km s}^{-1}$; see, e.g., Deguchi et al. 2004; Nakashima et al. 2004, 2015), and is also consistent with the median of intensity peak velocities of SiO, H_2O and OH maser emission (Nakashima et al. 2011, Note: Since SiO, H_2O and OH masers exhibit multiple intensity peaks with a strong time-variation in its profile, it is difficult to obtain the precise systemic velocity of the maser source, but the median velocity of maser emission (i.e., the averaged velocity of the highest and lowest velocity components) is consistent with that of thermal lines within several km s^{-1}). The intensity peak of the $\text{C}^{18}\text{O } J = 1-0$ line also seems to be consistent with the velocity of other molecular lines, though it is slightly shifted ($\sim 1 \text{ km s}^{-1}$) due presumably to the low signal-to-noise ratio. Although the $^{13}\text{CO } J = 1-0$ line exhibit 3 intensity peaks in its spectrum ($\sim 29.3 \text{ km s}^{-1}$, $\sim 35 \text{ km s}^{-1}$ and $\sim 44.5 \text{ km s}^{-1}$), the $\sim 29.3 \text{ km s}^{-1}$ and $\sim 44.5 \text{ km s}^{-1}$ components seem to be parts of extended cloudlet, which is not directly related to I19312. The $^{12}\text{CO } J = 1-0$ line does not show the intensity peak at $\sim 35 \text{ km s}^{-1}$, which is the systemic velocity of the central maser source of I19312. As discussed in our previous papers (see, e.g., Nakashima et al. 2004; Nakashima & Deguchi 2005), this seems to be due to the self absorption in the $^{12}\text{CO } J = 1-0$ line.

An interesting point seen in Figures 1 and 2 is that we see an arc-like (or bow-shock-like) structure in the velocities from 34.5 km^{-1} to 36.5 km^{-1} in Figure 1 and from 35.5 km^{-1} to 39.5 km^{-1} in Figure 2, and it is reminiscent of interacting regions, which are occasion-

ally found around mass-losing evolved stars (see, e.g., Ueta et al. 2006; Martin et al. 2007; Jorissen et al. 2011; Decin et al. 2012). In Figures 1 and 2, we indicated the crude location of the inner boundary of the arc-like structure by an ellipse, which is fit by eye inspection. We would like to note that this arc-like feature is also seen in the AKARI far infrared image (Kawada et al. 2007); see, Figure 5. The dashed straight lines in Figures 1 and 2 represent the long axis of the fitted ellipse. Interestingly, the position angle of the long-axis of the fitted ellipse (115°) is close to that of the jet axes of the H_2O maser jet (108° ; Nakashima et al. 2011) and CO molecular bipolar flow (130° ; Nakashima & Deguchi 2005), and it is also not largely different from the position angle of the symmetric axis of the near-infrared structure (143° ; Murakawa et al. 2007). Of course, this arc-like structure could be just extrinsic circumstances due to the inhomogeneity of the ambient gas and dust. However, as a possibility, such an arc-like structure of hydro dynamical interactions, can exist around a mass-losing evolved star. The detection of Class I methanol maser line (Nakashima et al. 2015) is also suggestive of the existence of an interaction/shock region around I19312. Later in Section 4.2, we give some more quantitative discussions about this possible arc-like structure.

Figure 6 shows the GRS maps of the ^{13}CO $J = 1-0$ line, which covers a region wider than that of Figures 1 and 2 (the map size of Figure 6 is $20' \times 20'$). We note that, even though here we present only a part of the velocity coverage of the GRS data cube, almost no CO emission are detected out of the velocity range of Figure 6 (the entire velocity coverage of the GRS data cube is from -5.0 km s^{-1} to 85.0 km s^{-1}). In Figures 5 and 6, we compare CO maps, the IRAS point source catalog (PSC) sources and AKARI far-infrared images (Kawada et al. 2007), so that we could reinspect the isolation of I19312, which is mentioned in Section 1 and our previous papers (see, e.g., Nakashima et al. 2011, 2015). Within $10'$ from the location of I19312, 7 IRAS PSC sources are found; the information of the nearby 7 IRAS sources are summarized in Table 2. Although we checked the SIMBAD database for these 7 IRAS sources, no significant information is found (except for IRAS measurements). In Figure 5 (AKARI far infrared image), we indicate the locations of the nearby 7 IRAS sources with the white crosses. As seen in Figure 5, except for IRAS 19309+1947, all other 6 IRAS sources do not have a clear counterpart in the AKARI far-infrared image; we see only extended cloudlet at the corresponding locations. In addition, the color of the cloudlet is significantly red in the image; this means that $160 \mu\text{m}$ emission is distinctly dominant (Note: $160 \mu\text{m}$ image represents red-color in the RGB color synthesis in Figure 5; the central wavelengths of the other two images used for the color synthesis are $90 \mu\text{m}$ [Green] and $60 \mu\text{m}$ [Blue]). In the Figure 6 (GRS ^{13}CO map), we see ^{13}CO emission at the locations of IRAS 19309+1947, IRAS 19308+1955 and IRAS 19306+1952. The GRS ^{13}CO spectra of these three sources are given in the lower panel in Figure 4. The CO emission of IRAS 19308+1955 and IRAS 19306+1952 is relatively weak and seems to be shapeless rather than

point-like. According to these properties, the IRAS sources in Table 2 (except for IRAS 19309+1947) are, most likely, not stellar-type objects, such as YSOs and dense cores, which must exhibit much clearer enhancements in CO and infrared flux densities. Presumably, what we are recognizing here as IRAS sources seems to be just the inhomogeneity of interstellar gas and dust.

On the other hand, in Figure 5 we clearly see an infrared point source at the location very close to the IRAS position of IRAS 19309+1947. We mentioned this object in our previous study (Nakashima et al. 2004). The IRAS [12]–[25] color ($1.56 - 2.5 \log F_{12}/F_{25} = 2.66$; here, F_{12} and F_{25} are IRAS 12 μm and 25 μm flux densities) is typical as a YSO, but the IRAS [25]–[60] color ($1.88 - 2.5 \log F_{25}/F_{60} = 5.32$; here, F_{25} and F_{60} are IRAS 25 μm and 60 μm flux densities) is out of the YSO range due to the large 60 μm flux (Straizys & Laugalys 2007). A search of the 6.7 GHz methanol maser emission was negative toward this object (Szymczak et al. 2000). The intensity peak velocity of this object, which is found in the lower panel in Figure 4, is shifted roughly 6 km s^{-1} away from that of I19312. This velocity shift seems to be somewhat large when we compare the value with a typical velocity dispersion of a star cluster (2 km s^{-1} – 3 km s^{-1} ; Nakashima & Deguchi 2006; Deguchi et al. 2010). At this moment, the true nature of this object is unclear, and moreover it is not clear whether this object is physically associated with I19312 or not.

4. Analysis

For better understanding the situation, in this section we obtain the following three values: (1) CO gas mass assuming the LTE condition, (2) a stellar velocity against to the interstellar medium assuming an analytic model of a bow shock, and (3) absolute luminosity using the latest archival photometric data and trigonometric parallax distance.

4.1. CO Gas Mass Assuming the LTE Condition

One of the original purposes of the present CO observation is to reveal the entire structure of the molecular component of I19312 and to derive the total mass of it. Here, we estimate the CO gas mass of the isolated molecular component of I19312. In order to obtain the gas mass, we firstly created a map of the CO column density and then derived the mass by summing up the column density within the emission region. The detailed procedure of the calculation is as follows.

Although we observed the $^{13}\text{CO } J = 1-0$, $^{12}\text{CO } J = 1-0$ and $\text{C}^{18}\text{O } J = 1-0$ lines, we

finally used only the $^{13}\text{CO } J = 1-0$ for the mass estimation. The C^{18}O data was excluded due simply to its low signal-to-noise ratio. The $^{12}\text{CO } J = 1-0$ line data was tentatively processed in the following way for trying to derive the excitation temperature, but we finally noticed that strong self-absorptions heavily disturbed the calculation as given the details later in this section, and did not use the data. (Anyway, in what follows, we describe the details of the analysis processes both about the $^{13}\text{CO } J = 1-0$ and $^{12}\text{CO } J = 1-0$.)

Since the beam size, velocity resolution, and grid sizes of the original data cubes are different in each line, we convolved the data cubes, so that both maps have the same beam and grid sizes. The pixel numbers, grid size, velocity resolution, and beam size of the convolved data cubes are $95 \times 101 \times 150$, $5'' \times 5''$, 1 km s^{-1} , $9.55''$, respectively. Then, we calculated the rms noise for each cube using emission free channels (specifically, we excluded velocities from 19.8 km s^{-1} to 49.8 km s^{-1} to avoid emission). The estimated rms noises are 0.33 K for ^{12}CO and 0.10 K for ^{13}CO .

We used the task GAUFIT in the Miriad software package (Sault et al. 1995) to fit the emission feature of the $^{13}\text{CO } J = 1-0$ and $^{12}\text{CO } J = 1-0$ lines in each pixel with a single Gaussian function. In this Gaussian fitting, we assumed following three points: (1) the minimum FWHM of the line is 1 km s^{-1} , (2) the minimum line intensity is 2σ , (3) the central velocity of the Gaussian function is in the range from 30.5 km s^{-1} to 38.5 km s^{-1} , which corresponds to the velocity range of the CO emission of I19312.

Since the line intensity, line width and central velocity of the line were calculated for each pixel, the output of the GAUFIT task was given as 2-dimensional maps of the obtained values. Additionally, we further convolved the maps of the line intensity, line width and the central velocity of the line with a $10''$ Gaussian beam to avoid artificial pixel-to-pixel sudden changes of the values.

After the Gaussian fitting, we calculated the column density distribution using the results of the Gaussian fitting. In principle, the excitation temperature (T_{ex}) was obtained from the main beam antenna temperature (T_{a}) of the ^{12}CO line, using the solution of the radiative transfer equation (equation 14.34 in Rohlfs & Wilson 2004). However, as stated above, in the present case it is impossible to derive the excitation temperature from the $^{12}\text{CO } J = 1-0$ due to the heavy self-absorption, which is lying over the systemic velocity of I19312. Thus, we assumed excitation temperatures for calculating the CO column density, so that we can estimate the mass only from the ^{13}CO line; specifically, we calculated the CO column density about 10 different temperatures, which are ranged from 10 K to 100 K with a 10 K step.

The optical depth of the $^{13}\text{CO } J = 1-0$ line is obtained with the following equation

(equation 15.31 in Rohlfs & Wilson 2004)

$$\tau(^{13}\text{CO}) = -\ln \left[1 - \frac{T_{\text{B}}^{13}}{5.3} \left\{ \left[\exp \left(\frac{5.3}{T_{\text{ex}}} \right) - 1 \right]^{-1} - 0.16 \right\}^{-1} \right],$$

where T_{B}^{13} is the brightness temperature of the ^{13}CO $J = 1-0$ line, T_{ex} is the excitation temperature. The source size of the compact component ($90''$ - $120''$, see Section 3 for details) is larger than beam size ($15''$), thus we can assume $T_{\text{B}} = T_{\text{mb}}$.

For linear, rigid rotor molecules such as CO or ^{13}CO , with the populations of all levels characterized by a single excitation temperature T_{ex} , the column density $N(^{13}\text{CO})$ and its optical depth τ are related as follows (equation 15.37 in Rohlfs & Wilson 2004)

$$N(^{13}\text{CO}) = 3.0 \times 10^{14} \frac{T_{\text{ex}}}{1 - \exp(-5.3/T_{\text{ex}})} \int \tau^{13}(v) dv \text{ (cm}^{-2}\text{)}.$$

In case of Gaussian line profile $\int \tau^{13}(v) dv = \tau_0^{13} \sigma_v \sqrt{2\pi}$, where σ_v – velocity dispersion of ^{13}CO line, τ_0 – optical depth in the center of the line. Column density of H_2 can be derived from abundance of $^{12}\text{CO}/^{13}\text{CO}$ and CO/H_2 :

$$N(\text{H}_2) = N(^{13}\text{CO}) \times \frac{^{12}\text{CO}}{^{13}\text{CO}} \times \left[\frac{\text{CO}}{\text{H}_2} \right]^{-1} \text{ (cm}^{-2}\text{)}.$$

According to the value given in Simon et al. (2001), we adopted the value of $\text{CO}/\text{H}_2 = 8 \times 10^{-5}$. As mentioned in Section 1, the trigonometric parallax distance to I19312 is about 3.8 kpc (Imai et al. 2011); with this distance, the galactocentric distance of I19312 can be calculated to be 6.9 kpc. At this galactocentric distance, according to Langer & Penzias (1990), the isotope ratio, $^{12}\text{CO}/^{13}\text{CO}$ is $\simeq 50$. Thus, for the calculation of the H_2 column density, we used the value $^{13}\text{CO}/\text{H}_2 = 1.6 \times 10^{-6}$. The mass is obtained by integrating the H_2 column densities over the source:

$$M = \mu m_{\text{H}_2} \int N_{\text{H}_2} dA,$$

where μ is the ratio of the interstellar gas mass to the mass of hydrogen molecule, $\mu \approx 1.33$ (Hildebrand 1983), m_{H_2} is the mass of hydrogen molecule. The surface element dA is related to the solid angle element $d\Omega$ by $dA = D^2 d\Omega$. If we combine previous three equations and constants, we can rewrite the equation for the gas mass in each pixel of the map with coordinate step $\Delta\alpha$ and $\Delta\delta$:

$$\frac{M}{M_{\odot}} \simeq 5.02 \times 10^{-25} D_{\text{kpc}}^2 \Delta\alpha'' \Delta\delta'' N_{\text{H}_2},$$

where N_{H_2} is the H_2 column density in each pixel of the map, $\Delta\alpha''$ and $\Delta\delta''$ – map step in arcseconds, D_{kpc} – distance to the source in kiloparsecs. We used following values for calculation: $D_{\text{kpc}} = 3.8$ kpc, $\Delta\alpha'' = \Delta\delta'' = 5''$. Mass is derived by summing the values from the each pixel of emission.

According to the CO feature found in the maps, we calculated the mass over a circle with a $40''$ radius, which is centered at the 2MASS position of I19312. Consequently, at the distance of 3.8 kpc, the mass of the source (the central isolated component of the I19312) is estimated to be in the range from 225 to 478 M_{\odot} ; the range of the estimated mass corresponds to the range of the excitation temperature from 10 to 40 K (see, footnote⁴). The results of the calculation are summarized in Table 3. One may think that the derived mass in the present study is far different from that estimated in previous studies (10–15 M_{\odot} ; see, e.g., Nakashima & Deguchi 2004, 2005). Here, we would like to note that Nakashima & Deguchi (2004) derived a gas mass using the data of a single-point observation using a single-dish telescope (i.e., they did not obtain a map), and therefore a non-negligible amount of emission of the central molecular component was missed from their observation; Note that their beam-size (HPBW) was about $15''$, while the integration region used in the present calculation is a circle with a $40''$ radius as we mentioned above. Therefore, the mass derived by Nakashima & Deguchi (2004) is only a part of the mass derived in the present work.

4.2. Stellar Velocity Assuming an Analytic Model of a Bow Shock

As mentioned in Section 3, we found a bow-shock-like structure in velocity channels close to the systemic velocity of I19312 (see, Figures 1 and 2). If we assume that this feature is a real bow-shock, which is formed by hydrodynamical interaction between the interstellar medium and the stellar wind of a moving star, we can estimate the relative velocity between the interstellar medium and the star under some assumptions about the

⁴Although we calculated the mass in the range from 10 to 100 K as given in Table 3, the averaged excitation temperature of the molecular component of I19312 does not seem to go beyond 40 K (presumably, much less than 40 K), because the size of the molecular component is relatively large ($5.1\text{--}6.8 \times 10^{18}$ cm), and also because the large size seems to prevent the heating the gas by the emission from the central star. Thus, here we give the mass corresponding to the temperature range of 10 – 40 K as a representative value

stellar wind parameters.

Assuming that the physical thickness of the shock shell is negligible and the ram pressure of the interstellar medium is balanced by that of the stellar wind, Wilkin et al. (1996) derived an analytic solution for the bow shock, which predicts that the distance between the apex and the central star (R_0) is given by the following formula.

$$R_0 = \sqrt{\dot{M}v_w / (4\pi\rho_{\text{ISM}}v_*^2)}$$

Here, \dot{M} is the mass-loss rate, v_w is the velocity of stellar wind, ρ_{ISM} is the mass density of the ISM, and v_* is the velocity of star respect to the interstellar medium. The shape of the bow shock can be expressed by the following formula.

$$R(\theta) = R_0 \sin^{-1} \theta \sqrt{3(1 - \theta \cot \theta)}$$

Here, θ is the polar angle from the symmetric axis as seen from the central star at the coordinate origin. Based on the present CO observations, we derive an angular separation between the apex of the bow and the star of $125''$. If we assume that the distance to this object is 3.8 kpc (Imai et al. 2011) and the symmetry axis of the bow shock lies in the sky plane, we obtain $R_0 = 7.1 \times 10^{18}$ cm. Assuming a low density atomic interstellar medium ($n_{\text{ISM}} = 0.1 \text{ cm}^{-3}$) and values for \dot{M} and v_w ($10^{-4} \text{ M}_\odot \text{ yr}^{-1}$ and 25 km s^{-1} , respectively, Nakashima et al. 2004; Nakashima & Deguchi 2005), we derive a stellar velocity of 11 km s^{-1} .

The linear size $R_0 = 7.1 \times 10^{18}$ cm corresponds to a distance of roughly 2.3 pc. This seems to be a relatively large distance, because for matter ejected from a star it takes about 9.0×10^4 yrs to reach such a distance (assuming the expansion velocity is 25 km s^{-1}) and the total mass ejected during this time (assuming the constant mass-loss rate $10^{-4 \sim -5} \text{ M}_\odot \text{ yr}$) would be 90 M_\odot . For comparison, the distance is much larger than the estimated distance to bow shock in AGB stars is only about 0.08 pc in case of R Hya (Ueta et al. 2006) to about 0.3 pc in Betelgeuse (Decin et al. 2012). We note that a remnant of an AGB wind, of which the size is about 1.3 pc, has been detected toward a planetary nebula NGC 7293 (Zhang et al. 2012); according to this size, it is not very unnatural even if hydrodynamical interactions are occurred at 1–2 pc away from the central star. If the central star of I19312 is/was a RSG as we discuss in Section 5, the mass-loss rate and the size of remnant stellar wind could be more immense.

4.3. Absolute Luminosity

In the past, we gave a couple of estimations about the absolute luminosity of I19312 (Nakashima et al. 2004, 2011). However, the recent results of the trigonometric parallax measurement with the VLBI technique (Imai et al. 2011) enables us to estimate a much more reliable value of the absolute luminosity, and furthermore many new photometric data have been released for the public. Here, we thoroughly collected photometric measurements of I19312, which are available for the public, and recalculated the absolute luminosity of I19312 using the most reliable distance information.

In order to construct the spectral energy distribution (SED) of I19312, we used the photometric data of the following observations, surveys, and archives: the optical INT/WFC Photometric H α Survey of the Northern Galactic Plane (IPHAS) i' -band magnitude, Two Micron All Sky Survey (2MASS), Near-infrared photometry at J , H , K and K_s bands from a ground-based observation (Nakashima et al. 2004), Mid-infrared images of the object were extracted from the *Spitzer* Galactic Legacy Infrared Mid-Plane Survey Extraordinaire (GLIMPSE), Wide-Field Infrared Survey Explorer (WISE), Infrared Astronomical Satellite (IRAS) Sky Survey, Midcourse Space Experiment (MSX), Multiband Imaging Photometer of Spitzer (MIPS), and AKARI IRC Survey. Many of the photometric data were obtained from the Data Discovery Service of the NASA/IPAC Infrared Science Archive⁵. The *Spitzer*/GLIMPSE fluxes were measured using the method described in Zhang et al. (2012) and Hsia & Zhang (2014). We used photometric data in the wavelength range between 0.763 μm and 2.096 mm (in total, 38 data points including upper limits). The photometric measurements collected are summarized in Table 4, and the SED diagram is given in Figure 6.

The optical-infrared photometric measurements are corrected based on two interstellar extinction coefficients toward I19312: i.e., $A(V) = 16.3$ (Frerking et al. 1982) and $A(V) = 30.98$ (Schlafly & Finkbeiner 2011). The extinction coefficients $A(V)$ were converted to $A(J)$ using the conversion factor given by Stead & Hoare (2009). Then, $A(\lambda)$ of corresponding wavelengths were derived based on Table 1 in Mathis (1990); we obtained the $A(\lambda)$ value by interpolating the values in Mathis (1990) when the conversion factor was not found at the corresponding wavelength (the correction does not change the values at wavelengths longer than roughly 4 μm).

The emerging flux of I19312 with extinction corrections are fitted by a three-component model using the same expression described in Hsia et al. (2010). As seen in Figure 6, only the

⁵<http://irsa.ipac.caltech.edu/cgi-bin/Radar/nph-estimation>

shortest wavelength component (less than roughly $\lambda = 5 \mu\text{m}$) is affected by the interstellar extinction correction. Since we have three cases of extinction corrections [i.e., $A(V) = 30.98$, 16.3, and 0], three temperatures of the fitted black bodies corresponding to each $A(V)$ value are obtained: i.e., those are $13,000 \pm 4,800 \text{ K}$ [$A(V) = 30.98$], $2,100 \pm 700 \text{ K}$ [$A(V) = 16.3$], and $1100 \pm 400 \text{ K}$ [$A(V) = 0$]. The first result (13,000 K) seems to be clearly too high as a temperature of a stellar maser source. This presumably means that the large extinction coefficient [$A(V) = 30.98$] is not reliable. The dust component is roughly fitted by two black bodies with temperatures of 191 K and 47 K. With an assumed distance of 3.8 kpc (Imai et al. 2011), we derived the total luminosity by integrating the region under the three black body models. The derived total luminosities are $2.06 \times 10^4 L_{\odot}$ [$A(V) = 0$], $2.63 \times 10^4 L_{\odot}$ [$A(V) = 16.3$], and $1.54 \times 10^6 L_{\odot}$ [$A(V) = 30.98$]. For the reason, mentioned above, presumably the absolute luminosity must be close to $2.63 \times 10^4 L_{\odot}$. In fact, this value is close to those given in other studies: i.e., $9.6 \times 10^3 L_{\odot}$ at 3.1 kpc (Cooper et al. 2013) and $1.37 \times 10^4 L_{\odot}$ at 3.7 kpc (Lumsden et al. 2013).

5. Discussion

As mentioned in Section 1, the primary purpose of the present research is to reveal the entire structure and mass of the molecular component of I19312 to constrain the possibilities of the origin of this complex system, which consists of a stellar maser source and chemically-rich molecular component. In the present observation, we revealed the entire structure of the molecular component of I19312, and we estimated the CO gas mass of the molecular component. In this section, we interpret the observational results given in Section 3 based on the analysis given in Section 4.

5.1. AGB/post-AGB stars and RSGs

As given in Section 4, the gas mass estimated in the present study is roughly ranged from 225 to 478 M_{\odot} (corresponding to the range of the excitation temperature from 10 to 40 K). Since we assumed the LTE and optically thin conditions for the $^{13}\text{CO } J = 1-0$ line, the estimated gas mass should be considered as the lower limit.

Our original question in the present research is whether the mass of the molecular component could be explained as materials expelled from a star (or a binary system consisting of stars). Although the bipolar molecular jet and extended infrared nebulosity of I19312 are reminiscent of those found in post-AGB stars and PPNe, which are the descendants of AGB

stars, the large gas mass far beyond $200 M_{\odot}$ never can be interpreted as materials expelled from a single AGB star, because the main-sequence mass of an AGB star is ranged roughly from $0.8 M_{\odot}$ to $8.0 M_{\odot}$ (see, e.g., Habing 1996; Busso et al. 1999). Even if assuming a binary system consisting of 2–3 AGB stars, it is still impossible to explain such a large mass. Thus, with the large estimated gas mass, first of all, we can safely conclude that the molecular component of I19312 is not originated in a single AGB star (or even a binary system consisting of 2-3 AGB stars). If the central SiO/H₂O/OH maser source is originated in an AGB/post-AGB star, the surrounding molecular component must be pre-existing rather than materials expelled from the central star. If this is to the case, the situation would be explained that the central AGB/post-AGB star coexists in a small isolated cloudlet with a mass of $225 M_{\odot} - 478 M_{\odot}$ and the star and the cloudlet share almost the same radial velocity of about 35 km s^{-1} . However, since the age of an AGB star is typically several Gyr (see, e.g., Olszewski et al. 1996; Guarnieri et al. 1997; Maciel et al. 2011), presumably it is impossible to consider that the natal molecular gas is still remained in the vicinity of the star over such a long time scale. Therefore, if the central stars is really an AGB/post-AGB star, we have to consider that the coexisting situation between the star and surrounding gas is a product of "pure chance".

Another major possibility of explaining a mass-losing evolved star must be an RSG. The observational properties of RSGs are, in many aspects, quite similar to those of AGB stars. For example, infrared colors of RSGs are basically the same with those of AGB stars, because the dust temperature is almost the same (see, e.g., Fok et al. 2012). RSGs exhibit a circumstellar envelope, which is often similar to that found in AGB/post-AGB stars in nature (see, e.g., Shinnaga et al. 2003). Maser properties of RSGs are also similar to those of AGB stars, although the velocity ranges of maser emission of RSGs are somewhat larger than those of AGB stars (Nakashima & Deguchi 2007; Deguchi et al. 2010; Fok et al. 2012). But, an important difference between RSGs and AGB/post-AGB stars are the initial mass. An RSG has a larger initial mass than an AGB star: its mass-range is roughly from $10 M_{\odot}$ to $25 M_{\odot}$ (Levesque 2009). And, therefore, the age of RSGs are much shorter than AGB stars: say, < 20 million years (see, e.g., Davies et al. 2007, 2008). Even if we assume the initial mass of $10 M_{\odot} - 25 M_{\odot}$, however, all the mass of the molecular component (225 to $478 M_{\odot}$) cannot be explained as materials expelled from an RSG or a binary system including 2-3 RSGs (putting aside whether such a binary system is physically possible) as well as the case of AGB/post-AGB stars. Therefore, the molecular component, anyway, must be pre-existing even if we assume an RSG. However, since the age of RSGs are much younger than AGB stars, the surrounding materials could be still a natal cloud (or a remnant of natal cloud) for the central RSG. In fact, in some open clusters containing RSGs still posses molecular component, which could be a natal cloud of RSGs (Deguchi et al. 2010). In such a case,

however, presumably there should be a concentration of stars, which are formed in the same natal cloud, but there is no such a concentration of stars found so far around I19312. [Note: in a high-resolution HST/WFC image, we find a weak concentration of several stars in the vicinity of a red star (within roughly $3.5''$), which seems to be the source of SiO/H₂O/OH masers. But, it is not clear whether these stars have a physical relation with the central maser source.] In terms of the luminosity, the value derived in Section 4.3 ($2.63 \times 10^4 L_{\odot}$) is consistent with the case of an RSG (Wood et al. 1983; Groenewegen et al. 2009; Fok et al. 2012), although it is also not very inconsistent with the upper limit of post-AGB stars (Reyniers & Van Winckel 2001; Whitelock & Marang 2001; van Winckel 2003). For those reasons, at this moment, an RSG, which is embedded in the (remnant of) natal cloud, seems to be more preferable interpretation for I19312 compared to the case of AGB/post-AGB stars lying in a small molecular component by pure chance, although not all the observational properties are consistently explained yet.

5.2. Other Possibilities and Related Issues

In terms of the large mass of the molecular component, one may think that a mass-loss of a very massive star with an initial mass of $100 M_{\odot} - 200 M_{\odot}$ could form a surrounding molecular component with a mass nearly equivalent to the stellar mass. In fact, a dozen of stars with a quite large initial-mass more than $100 M_{\odot}$ are known in the sky: for example, R136a1, R136a2, R136a3, NGC 3603-B, R136c, NGC 3603-C (Crowther et al. 2010), HD 269810 (Walborn et al. 1995), VFTS 682 (Vink et al. 2012), WR42e (Gvaramadze et al. 2013). However, the situation of such extreme massive stars seems to be far different from the case of I19312. The most importantly, such very massive stars definitely exhibit high-energy phenomena, such as X-ray emission and extremely high outflow-velocity, due to its large self gravity (see, e.g., Seward et al. 1979; Damini Neto et al. 1993; Townsley et al. 2006), developing an ionized region around the star (see, e.g., Okamoto et al. 2003; Jamet et al. 2004). These are not the case for I19312: an ionized region has not been detected so far, for example, in a B γ imaging and free-free emission surveys (Nakashima et al. 2004, 2011).

In our previous papers, we discussed a possibility of a merger of two main-sequence stars (or two stars going to the main-sequence) for explaining the situation of I19312 (see, e.g., Nakashima et al. 2011). Specifically, we pointed out some similarities between I19312 and V838 Mon (Nakashima et al. 2011): i.e., V838 Mon exhibits both SiO masers and extended nebulosity, which is detected in the CO radio lines, as well as I19312 does (Deguchi et al. 2005; Kaminski et al. 2007; Kaminski 2008). Therefore, the most promising model explaining the observational properties of V838 Mon seems to be the merger of two stars (see, e.g.,

Soker & Tylenda 2007). However, the present result suggests that the surrounding gas of I19312 (roughly, 225 to 478 M_{\odot}) is much larger than that of V838 Mon (a few tens of solar masses, Kaminski 2008), and such a large mass cannot be explained by the gas expelled from the two merging stars. Even in such a case, we still could assume that the SiO maser emission of I19312 are caused by the merger of two stars as well as V838 Mon, but to explain the merger, presumably we should see a dense stellar concentration around the merging stars, otherwise two stars have no chance (or very small chance) to meet to merge. In fact, Afşar & Bond (2007) found that V838 Mon is a member of a B-stars association and the narrow CO emission can be attributed to an interstellar medium within the cluster. However, such a clear star association is not found in the vicinity of I19312 so far, as partly mentioned in Section 5.1.

As we discussed in Section 5.1, if the molecular component of I19312 is a part of the natal cloud of an RSG with masers, another concern would be which parts of the CO emission found in Figures 1, 2 and 6 is the same natal cloud, which formed the RSG. As we calculated in Section 4.2, if we assume the arc-like feature seen in Figures 1 and 2 is caused by a bow-shock, the relative velocity is calculated to be 11 km s^{-1} . This relative velocity seems to be too large as a velocity dispersion of a single natal cloud, which forms RSGs. In fact, the velocity dispersion of an open cluster including RSGs are, at most, roughly $\sim 5 \text{ km s}^{-1}$ (typically, $2 \text{ km s}^{-1} - 3 \text{ km s}^{-1}$; Nakashima & Deguchi 2006; Deguchi et al. 2010). Therefore, if we believe that the bow shock is a real existence, the molecular gas lying in the south-east of I19312 is probably not directly related to the formation of the RSG in I19312.

6. Summary

We have reported the results of a wide field CO mapping in the region of I19312. We revealed the entire structure of the molecular component of I19312 for the first time. We calculated CO gas mass assuming the LTE condition, a stellar velocity against to the interstellar medium assuming an analytic model of a bow shock, and absolute luminosity using the latest archival photometric data and trigonometric parallax distance. The derived large gas-mass and relatively large luminosity suggests that the central SiO/H₂O/OH maser source seems to be an RSG rather than an AGB/post-AGB star, and the surrounding molecular component could be a natal cloud of an RSG.

This work is supported by Act 211 Government of the Russian Federation, agreement No. 02.A03.21.0006. YZ thanks the Hong Kong General Research Fund (HKU7073/11P) for the financial support of this study. Nobeyama Radio Observatory is a branch of the

National Astronomical Observatory of Japan, National Institutes of Natural Sciences. We thank Sergey Y. Parfenov for stimulating discussions about the infrared high-dispersion spectroscopy of IRAS 19312+1950 and the infrared sources in the surveyed region. We also thank Shuji Deguchi and Wayne Chau for their extensive help in the NRO observation.

REFERENCES

- Afşar, M., & Bond, H. E. 2007, *AJ*, 133, 387
- Aguirre, J. E., et al. 2011, *ApJS*, 192, id. 4
- Barentsen, G., Farnhill, H. J., & Drew, J. E. et al. 2014, *MNRAS*, 444, 3230
- Barvainis, R., & Clemens, D. P. 1984, *AJ*, 89, 1833
- Busso, M., Gallino, R., & Wasserburg, G. J. 1999, *ARA&A*, 37, 239
- Cernicharo, J., Guelin, M., & Kahane, C. 2000, *A&AS*, 142, 181
- Charnley, S. B., & Latter, W. B. 1997, *MNRAS*, 287, 538
- Cooper, H. D. B., Lumsden, S. L., Oudmaijer, R. D., 2013, *MNRAS*, 430, 1125
- Crowther, P. A., Schnurr, O., Hirschi, R., Yusof, N., Parker, R. J., Goodwin, S. P., & Kassim, H. A. 2010, *MNRAS*, 408, 731
- Csengeri, T., Urquhart, J. S., Schuller, F., et al. 2014, *A&A*, 565, A75
- Cutri, R. M., Skrutskie, M. F., van Dyk, S., et al. 2003, *VizieR Online Data Catalog*, II/246
- Cutri, R. M., Wright, E. L., Conrow, T., et al. 2012, *yCat*, 2311, 0
- Damineli Neto, A., Viotti, R., Baratta, G. B., & de Araujo, F. X. 1993, *A&A*, 268, 183
- Davies, B., Figer, D. F., Kudritzki, R.-P., MacKenty, J., Najarro, F., & Herrero, A. 2007, *ApJ*, 671, 781
- Davies, B., Figer, D. F., Law, C. J., Kudritzki, R.-P., Najarro, F., Herrero, A., & MacKenty, J. W. 2008, *ApJ*, 676, 1016
- Decin, L., et al. 2012, *A&A*, 548, A113
- Deguchi, S., et al. 2004, *PASJ*, 56, 261

- Deguchi, S., Matsunaga, N., & Fukushi, H. 2005, PASJ, 57, L25
- Deguchi, S., Nakashima, J., & Takano, S. 2004, PASJ, 56, 1083
- Deguchi, S., Nakashima, J., Zhang, Y., Chong, S. S. N., Koike, K., & Kwok, S. 2010, PASJ, 62, 391
- Dunham, M. K., Rosolowsky, E., Evans, N. J., II, Cyganowski, C., & Urquhart, J. S. 2011, ApJ, 741, 110
- Egan, M. P., Price, S. D., Kraemer, K. E., et al. 2003, The Midcourse Space Experiment Point Source Catalog v2.3, Air Research Laboratory Technical Report AFRL-VS-TR-2003-1589
- Emerson, D. T., & Graeve, R. 1988, A&A, 190, 353
- Fok, T. K. T., Nakashima, J., Yung, B. H. K., Hsia, C.-H., & Deguchi, S. 2012, ApJ, 760, 65
- Frerking, M. A., Langer, W. D., & Wilson, R. W. 1982, ApJ, 262, 590
- Genzel, R., Downes, D., Schwartz, P. R., Spencer, J. H., Pankonin, V., & Baars, J. W. M. 1980, ApJ, 239, 519
- Gomez, J. F., Uscanga, L., Suarez, O., Rizzo, J. R., & de Gregorio-Monsalvo, I. 2014, Rev. Mexicana Astron. Astrofis., 50, 137
- Groenewegen, M. A. T., Sloan, G. C., Soszynski, I., & Peterson, E. A. 2009, A&A, 506, 1277
- Guarnieri, M. D., Renzini, A., & Ortolani, S. 1997, ApJ, 477, L21
- Gvaramadze, V. V., Kniazev, A. Y., Chene, A.-N., & Schnurr, O. 2013, MNRAS, 430, L20
- Habing, H. J. 1996, A&A Rev., 7, 97
- Hasegawa, T., Morita, K., Okumura, S., Kaifu, N., Suzuki, H., Ohishi, M., Hayashi, M., & Ukita, N. 1986, in Proc. Masers, Molecules and Mass Outflows in Star Forming Regions, ed. A. D. Haschick (Westford: Haystack Obs.), 275
- He, J. H., et al. 2008, ApJS, 177, 275
- Hildebrand, R. H. 1983, QJRAS, 24, 267
- Hsia, C.-H., Kwok, S., Zhang, Y., Koning, N., & Volk, K. 2010, ApJ, 725, 173

- Hsia, C.-H. & Zhang, Y. 2014, *A&A*, 563, A63
- Imai, H., Obara, K., Diamond, P. J., Omodaka, T., & Sasao, T. 2002a, *Nature*, 417, 829
- Imai, H., et al. 2002b, *PASJ*, 54, L19
- Imai, H., Tafuya, D., Honma, M., Hirota, T., & Miyaji, T. 2011, *PASJ*, 63, 81
- Ishihara, D., Onaka, T., Kataza, H., et al. 2010, *A&A*, 514, A1
- Jackson, J. M., et al. 2006, *ApJS*, 163, 145
- Jamet, L., Perez, E., Cervino, M., Stasiska, G., Gonzalez Delgado, R. M., & Vilchez, J. M. 2004, *A&A*, 426, 399
- Jewell, P. R., Batrla, W., Walmsley, C. M., & Wilson, T. L. 1984, *A&A*, 130, L1
- Jorissen, A., et al. 2011, *A&A*, 532, A135
- Kaminski, T. 2008, *A&A*, 482, 803
- Kaminski, T., Miller, M., & Tylenda, R. 2007, *A&A*, 569
- Kawada, M., et al. 2007, *PASJ*, 59, S389
- Kawaguchi, K., Kasai, Y., Ishikawa, S., & Kaifu, N. 1995, *PASJ*, 47, 853
- Langer, W. D., & Penzias, A. A. 1990, *ApJ*, 357, 477
- Levesque, E. M. 2009, *ASPC*, 425, 103
- Lovas, F. J., 1992, *Journal of Physical and Chemical Reference Data*, 21, 181
- Lumsden, S. L., et al. 2013, *ApJS*, 208, id. 11
- Maciel, W. J., Costa, R. D. D., & Idiart, T. E. P. 2011, *ASP Conf Ser*, 445, 343
- Mathis, J. S. 1990, *ARA&A*, 28, 37
- Martin, D. C., et al. 2007, *Nature*, 448, 780
- Moshir, M., Kopman, G., & Conrow, T. A. O. (ed.) 1992, *IRAS Faint Source Survey, Explanatory Supplement Version 2*
- Mottram, J. C., Hoare, M. G., Lumsden, S. L., et al. 2010, *A&A*, 510, A89
- Murakawa, K., Nakashima, J., Ohnaka, K., & Deguchi, S. 2007, *A&A*, 470, 957

- Nakashima, J., & Deguchi, S. 2000, PASJ, 52, L43
- Nakashima, J., Jiang, B. W., Deguchi, S., Sadakane, K., & Nakada, Y. 2000, PASJ, 52, 275
- Nakashima, J., & Deguchi, S. 2005, ApJ, 633, 282
- Nakashima, J., & Deguchi, S. 2006, ApJ, 647, L139
- Nakashima, J., & Deguchi, S. 2007, ApJ, 669, 446
- Nakashima, J., Deguchi, S., Imai, H., Kembball, A., & Lewis, B. M. 2011, ApJ, 728, 76
- Nakashima, J., & Deguchi, S. 2004, ApJ, 610, L41
- Nakashima, J., Deguchi, S., & Kuno, N. 2004, PASJ, 56, 193
- Nakashima, J., Sobolev, A. M., Saliu, S., Deguchi, S., Yung, B. H. K., Zhang, Y. 2015, PASJ, 67, 95
- Okamoto, Y. K., et al. 2003, ApJ, 584, 368
- Olszewski, E. W., Suntzeff, N. B., & Mateo, M. 1996, ARA&A, 34, 511
- Planck Collaboration XXVIII. 2014, A&A, 571, A28
- Reyniers, M., & Van Winckel, H. 2001, A&A, 365, 465
- Rohlfs, K., & Wilson, T. L. 2004, Tools of radio astronomy (Springer-Verlag, Heidelberg)
- Rosolowsky, E., Dunham, M. K., Ginsburg, A., et al. 2010, ApJS, 188, 123
- Sault, R. J., Teuben, P. J., & Wright, M. C. H. 1995, Astronomical Data Analysis Software and Systems IV, ASP Conference Series, eds, Shaw, R A, Payne, H E and Hayes, J J E, 77, 433
- Sawada, T., et al. 2008, PASJ, 60, 445
- Scoville, N. Z., Sargent, A. I., Sanders, D. B., Claussen, M. J., Masson, C. R., Lo, K. Y., & Phillips, T. G. 1986, ApJ, 303, 416
- Schlaafy, E. F., & Finkbeiner, D. P. 2011, ApJ, 737, 103
- Schlegel, D. J., Finkbeiner, D. P., & Davis, M. 1998, ApJ, 500, 525
- Seward, F. D., Forman, W. R., Giacconi, R., Griffiths, R. E., Harnden, F. R., Jr., Jones, C., & Pye, J. P. 1979, ApJ, 234, L55

- Shinnaga, H., Claussen, M. J., Lim, J., Trung, D. V., & Tsuboi, M. 2003, *ASSL*, 283, 393
- Shirley, Y. L., et al. 2013, *ApJS*, 209, id. 2
- Simon, R., Jackson, J. M., Clemens, D. P., Bania, T. M., & Heyer, M. H. 2001, *ApJ*, 551, 747
- Soker, N., & Tytenda, R. 2007, *ASPC*, 363, 280
- Sorai, K., Sunada, K., Okumura, S. K., Tetsuro, I., Tanaka, A., Natori, K., Onuki, H., 2000 *Proc. SPIE*, 4015, 86
- Stead, J. J., & Hoare, M. G. 2009, *MNRAS*, 400, 731
- Straižys, V., & Laugalys, V. 2007, *Baltic Astronomy*, 16, 327
- Sunada, K., Yamaguchi, C., Nakai, N., Sorai, K., Okumura, S. K., Ukita, N. 2000, *Proc. SPIE*, 4015, 237
- Szymczak, M., Hrynek, G., & Kus, A. J. 2000, *A&AS*, 143, 269
- Townsley, L. K., Broos, P. S., Feigelson, E. D., Garmire, G. P., & Getman, K. V. 2006, *AJ*, 131, 2164
- Ueta, T., et al. 2006, *ApJ*, 648, L39
- van Winckel, H. 2003, *ARA&A*, 41, 391
- Vink, J. S., Bestenlehner, J. M., Grafener, G., de Koter, A., & Langer, N. 2012, *ASP Conference Series*, 465, 207
- Walborn, N. R., Long, K. S., Lennon, D. J., & Kudritzki, R.-P. 1995, *ApJ*, 454, L27
- Whitelock, P., & Marang, F. 2001, *MNRAS*, 323, L13
- Wienen, M., Wyrowski, F., Schuller, F., et al. 2012, *A&A*, 544, A146
- Wilkin, F. P. 1996, *ApJ*, 459, L31
- Wood, P. R., Bessel, M. S., & Fox, M. W. 1983, *ApJ*, 272, 99
- Yamaguchi, C., Sunada, K., Iizuka, Y., Iwashita, H., Noguchi, T., 2000, *Proc. SPIE*, 4015, 614
- Yung, B. H. K., Nakashima, J., Imai, H., Deguchi, S., Diamond, P. J., & Kwok, S. 2011, *ApJ*, 741, 94

Yung, B. H. K., Nakashima, J., Imai, H., Deguchi, S., Henkel, C., & Kwok, S. 2013, *ApJ*, 769, 20

Yung, B. H. K., Nakashima, J., & Henkel, C. 2014, *ApJ*, 794, 81

Zhang, Y., Hsia, C. -H., & Kwok, S. 2012, *ApJ*, 745, 59

Table 1. Summary of observational parameters

	$^{12}\text{CO } J = 1-0$	$^{13}\text{CO } J = 1-0$	$\text{C}^{18}\text{O } J = 1-0$
Rest frequency* (GHz)	115.271202	110.201354	109.782176
Mapped region	$500'' \times 500''$	$500'' \times 500''$	$250'' \times 250''$
Scan number (X-direction)	3	12	5
Scan number (Y-direction)	2	11	4
Velocity coverage (km s^{-1})	± 666.3	± 696.9	± 700.0
Velocity resolution (km s^{-1})	1.30	1.36	1.37
r.m.s. noise (K)	2.13×10^{-1}	6.05×10^{-2}	9.85×10^{-2}

*Rest frequencies are taken from Lovas (1992).

Table 2. IRAS PSC sources within $10'$ from IRAS 19312+1950

IRAS name	F_{12} (Jy)	F_{25} (Jy)	F_{60} (Jy)	Separation ($''$)	CO emission km s^{-1}
19306+1952	1.40	0.49	3.93	562	26.5–28.5, 33.5–34.5
19308+1955	1.00	0.59	3.93	459	27.5–28.5, 40.5–43.5
19309+1947	1.22	15.40	366.10	291	27.5–32.5
19310+1959	1.71	1.08	1.87	547	no CO emission
19311+1941	0.62	1.23	4.44	537	no CO emission
19313+1958	0.96	0.39	4.00	490	no CO emission
19316+1944	0.56	0.42	2.79	548	no CO emission

Note. — F_{12} , F_{25} and F_{60} are IRAS flux densities at $12 \mu\text{m}$, $25 \mu\text{m}$ and $60 \mu\text{m}$.

Table 3. Results of the LTE Mass Estimation

T_{ex} (K)	$\tau(^{13}\text{CO})$	$N(\text{CO})$ 10^{16} cm^{-2}	$N(\text{H}_2)$ 10^{22} cm^{-2}	Mass (M_{\odot})
10	0.32	1.02	0.63	225
20	0.12	1.31	0.82	290
30	0.07	1.73	1.08	382
40	0.05	2.16	1.35	478
50	0.04	2.61	1.62	576
60	0.03	3.05	1.91	674
70	0.028	3.50	2.19	773
80	0.024	3.95	2.47	872
90	0.018	4.40	2.75	971
100	0.016	4.84	3.03	1070

Note. — T_{ex} : excitation temperatures assumed, $\tau(^{13}\text{CO})$: mean ^{13}CO optical depths of the source, $N(\text{CO})$ and $N(\text{H}_2)$: column densities of CO and H_2 , respectively, Mass: derived masses.

Table 4. Photometric Measurements of IRAS 19312+1950

Measurements (flux unit)	Flux values	Reference
Optical data		
IPHAS i' (mag)	18.11±0.04	Barentsen et al. (2014)
Infrared data		
2MASS J (mag)	11.332±0.029	Cutri et al. (2003)
2MASS H (mag)	7.718±0.024	Cutri et al. (2003)
2MASS K_s^a (mag)	6.615	Cutri et al. (2003)
J (mag)	10.7±0.1	Nakashima et al. (2004)
H (mag)	7.80±0.1	Nakashima et al. (2004)
K (mag)	6.30±0.1	Nakashima et al. (2004)
WISE 3.4 μm (Jy)	4.365±0.076	Cutri et al. (2012)
WISE 12 μm (Jy)	0.253±0.01	Cutri et al. (2012)
WISE 22 μm (Jy)	2.122±0.002	Cutri et al. (2012)
Spitzer 3.6 μm^b (Jy)	2.65±0.46	This study
Spitzer 4.5 μm^b (Jy)	3.21±0.58	This study
Spitzer 5.8 μm^b (Jy)	11.42±1.67	This study
Spitzer 8.0 μm^b (Jy)	10.52±1.33	This study
MSX 8.3 μm (Jy)	11.84±0.49	Egan et al. (2003)
MSX 12.1 μm (Jy)	22.68±1.13	Egan et al. (2003)
MSX 14.7 μm (Jy)	23.08±1.41	Egan et al. (2003)
MSX 21.3 μm (Jy)	45.00±2.70	Egan et al. (2003)
IRAS 12 μm (Jy)	22.61±0.95	Moshir et al. (1992)
IRAS 25 μm (Jy)	69.77±2.73	Moshir et al. (1992)
IRAS 60 μm (Jy)	317.60±17.15	Moshir et al. (1992)
IRAS 100 μm (Jy)	427.00±21.35	Moshir et al. (1992)
AKARI 9 μm (Jy)	13.71±0.14	Ishihara et al. (2010)
AKARI 18 μm (Jy)	37.02±0.45	Ishihara et al. (2010)
AKARI 65 μm (Jy)	313.10±29.40	Ishihara et al. (2010)
AKARI 90 μm (Jy)	176.30±38.90	Ishihara et al. (2010)
AKARI 140 μm (Jy)	302.90±42.00	Ishihara et al. (2010)
AKARI 160 μm (Jy)	275.10±31.80	Ishihara et al. (2010)
IRAS IGA 60 μm (Jy)	379.62±0.68	Mottram et al. (2010)
Spitzer MIPS 70 μm (Jy)	556.13±3.07	Mottram et al. (2010)
IRAS IGA 100 μm (Jy)	303.13±6.55	Mottram et al. (2010)
ATLASGAL 870 μm (Jy)	2.79	Csengeri et al. (2014)
ATLASGAL F 870 μm (Jy)	2.45	Wienen et al. (2012)
BGPS 1100 μm (Jy)	1.18±0.16	Dunham et al. (2011)
BGPS 1100 μm (Jy)	1.186±0.21	Rosolowsky et al. (2010)
Radio data		
Planck 857 GHz (mJy)	98525±8330.75	Planck Collaboration XXVIII (2014)
Planck 143 GHz (mJy)	802.97±132.53	Planck Collaboration XXVIII (2014)
RMS 5 GHz ^c (mJy)	0.7	Cooper et al. (2013)

^aNote that the 2mass K_s band flux is unreliable.

^bMeasured from Spitzer GLIMPSE images.

^cNote that the flux measured from 5 GHz is an upper limit.

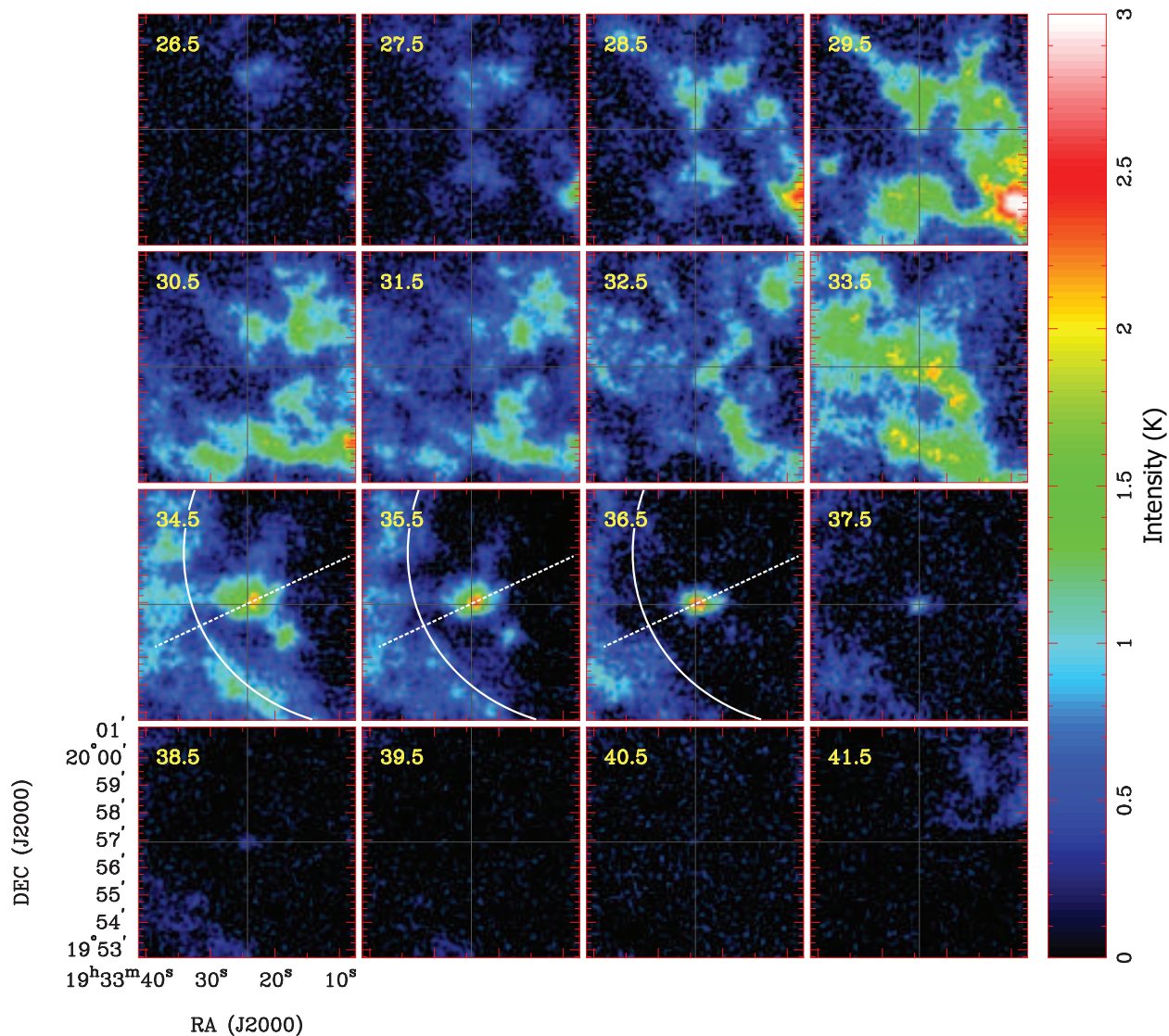


Fig. 1.— Velocity-Channel maps of the $^{13}\text{CO } J = 1-0$ line. The data were taken by the BEARS camera mounted on the NRO 45m telescope. The radial velocity (V_{lsr}) is given in the upper-left corners of each panel. The color intensity scale in K is given on the right side of the channel maps. The intersection of the gray vertical and horizontal lines represents the location of IRAS 19312+1950 (2MASS position). The white curve (a part of an ellipse) indicates the inner boundary of a possible bow-shock feature, and the white broken line represents the long axis of the ellipse.

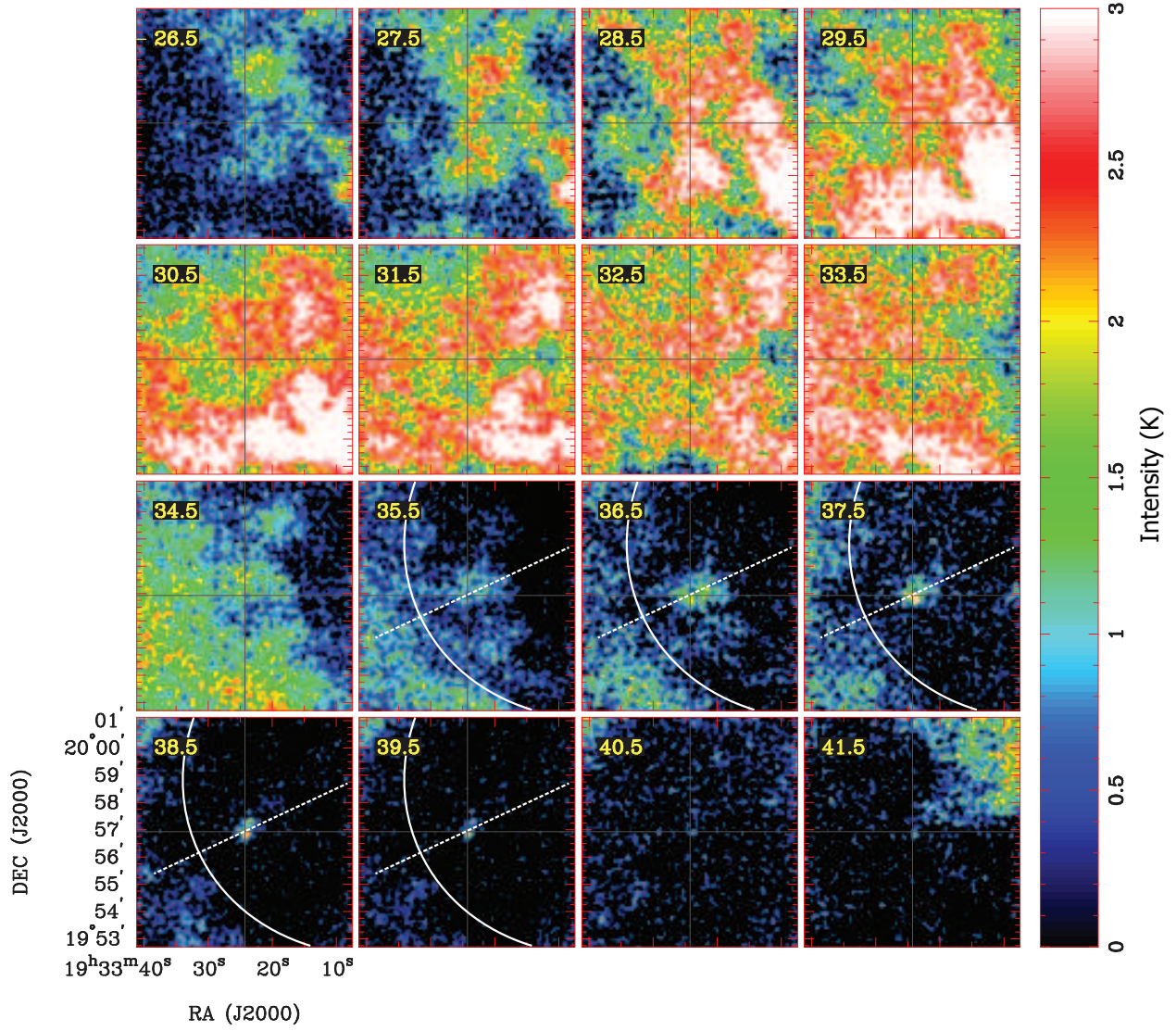


Fig. 2.— Velocity-Channel maps of the $^{12}\text{CO } J = 1-0$ line. The notations of the figure is the same as Figure 1.

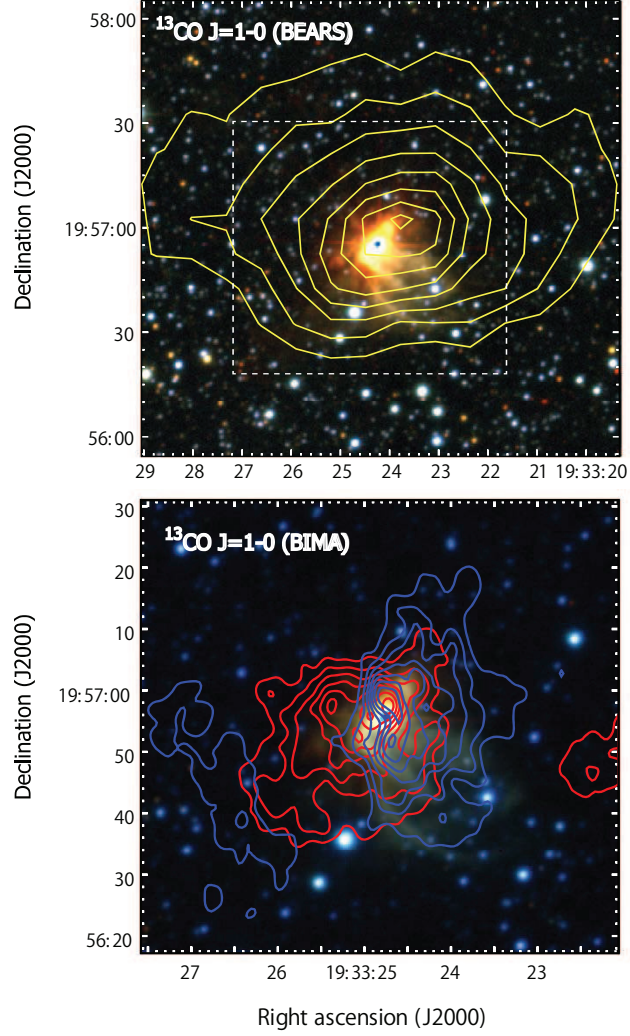


Fig. 3.— **Upper panel:** velocity-integrated intensity map of the $^{13}\text{CO } J = 1-0$ line. The data was taken by the BEARS camera mounted on the NRO 45m telescope. The background is the J , H , K -bands composite color image of the UKIDSS data (both for the upper and lower panels). The velocity range for the integration is from 34.5 km s^{-1} to 39.5 km s^{-1} . The contour levels start from 2.0 K km s^{-1} , and the levels are spaced every $0.871 \text{ K km s}^{-1}$. The highest contour corresponds to 8.1 K km s^{-1} . The white dashed square represents the size of the lower panel. **Lower panel:** velocity-integrated intensity map of the $^{13}\text{CO } J = 1-0$ line. The data were taken by the BIMA array (Nakashima & Deguchi 2005). The blue contours represent the velocity ranges of $35-36 \text{ km s}^{-1}$, and the red contours represent the velocity ranges of $37-38 \text{ km s}^{-1}$. The contour levels start from 1.0 Jy beam^{-1} , and the levels are spaced every $0.77 \text{ Jy beam}^{-1}$.

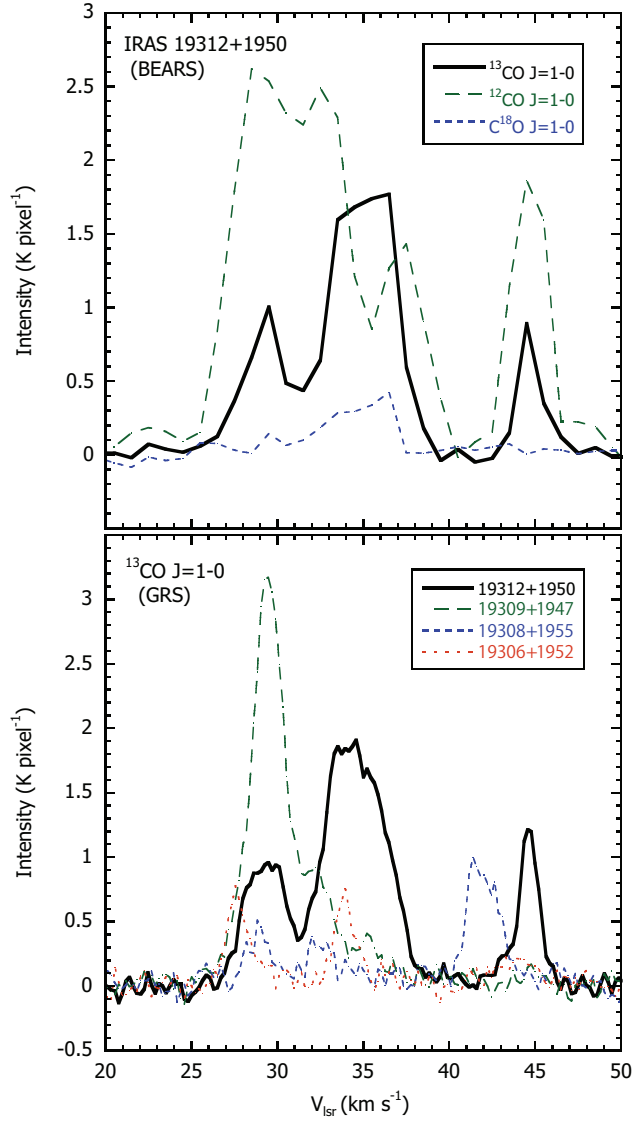


Fig. 4.— **Upper panel:** Spatially integrated BEARS spectra of the $^{13}\text{CO } J = 1-0$ (thick black line), $^{12}\text{CO } J = 1-0$ (green broken line) and $\text{C}^{18}\text{O } J = 1-0$ (blue broken line) lines toward IRAS 19312+1950. The integration region is a circle with a radius of $25''$, which is centered at the 2MASS position of IRAS 19312+1950. **Lower panel:** Spatially integrated GRS spectra of the $^{13}\text{CO } J = 1-0$ line toward IRAS 19312+1950 (thick black line), IRAS 19309+1947 (green broken line), IRAS 19308+1955 (blue broken line) and IRAS 19306+1952 (orange dotted line). The integration regions are circles with a radius of $25''$, which are centered at each IRAS position (for IRAS 19312+1950 and IRAS 19309+1947, the 2MASS and AKARI positions are respectively used).

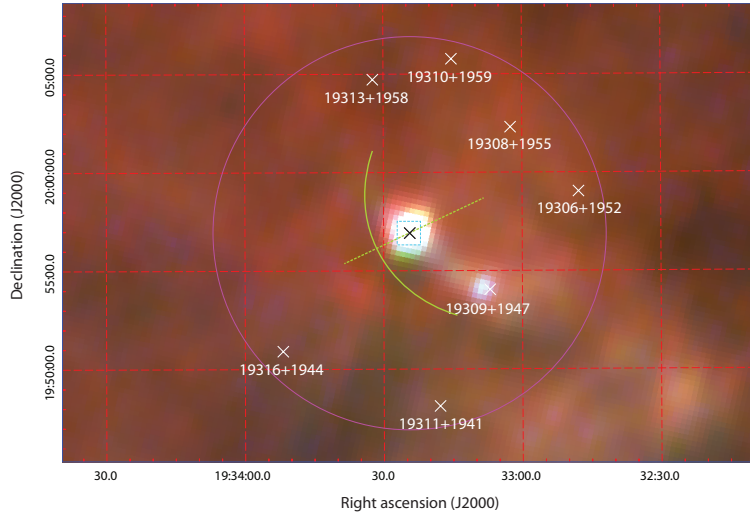


Fig. 5.— Composite color image of the AKARI far-infrared images. The AKARI N60 ($60 \mu\text{m}$; blue), WideS ($90 \mu\text{m}$; green) and N160 ($160 \mu\text{m}$; red) images were combined to create the false RGB color. The black cross represents the location of I19312, and the white crosses represent the locations of nearby IRAS sources found within $10'$ from I19312. The magenta circle with a radius of $10'$, which is centered at I19312, is given as an indicator for the angular distance from I19312. The light green curve and broken line are the same with the white curve and broken line given in Figures 1 and 2 (i.e., the inner boundary of a possible bow-shock feature and the axis of the structure). The blue square corresponds to the white dashed square given in the upper panel in Figure 3 (i.e., the size of the BIMA map given in the lower panel in Figure 3).

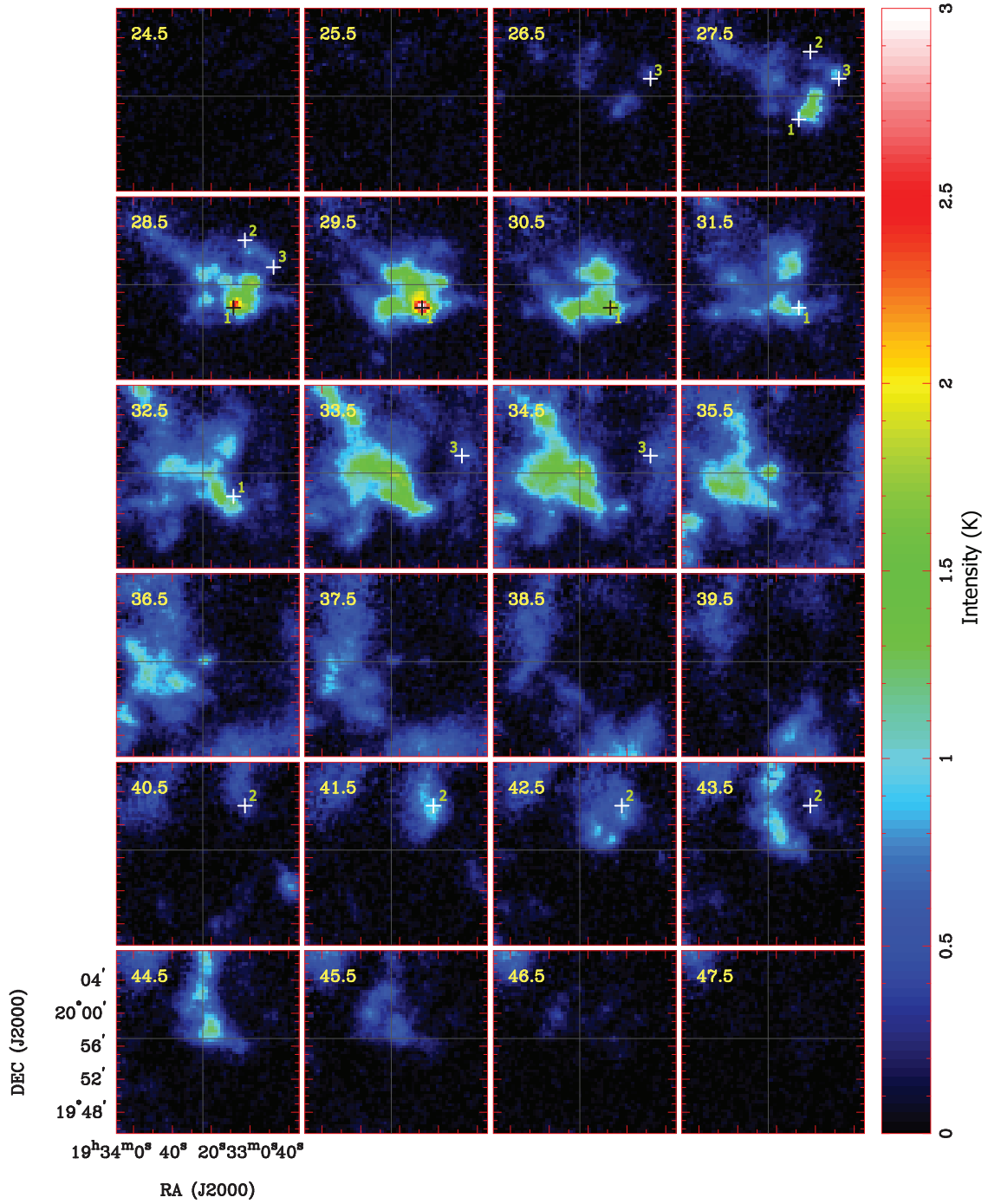


Fig. 6.— Velocity-Channel maps of the $^{13}\text{CO } J = 1-0$ line. The data were taken from the GRS data archive. The crosses with identification numbers indicate the location of IRAS point sources within $10'$ from IRAS 19312+1950. The identification number 1, 2 and 3 corresponds to IRAS 19309+1947, IRAS 19308+1955 and IRAS 19306+1952. The other notations of the figure is the same as Figure 1.

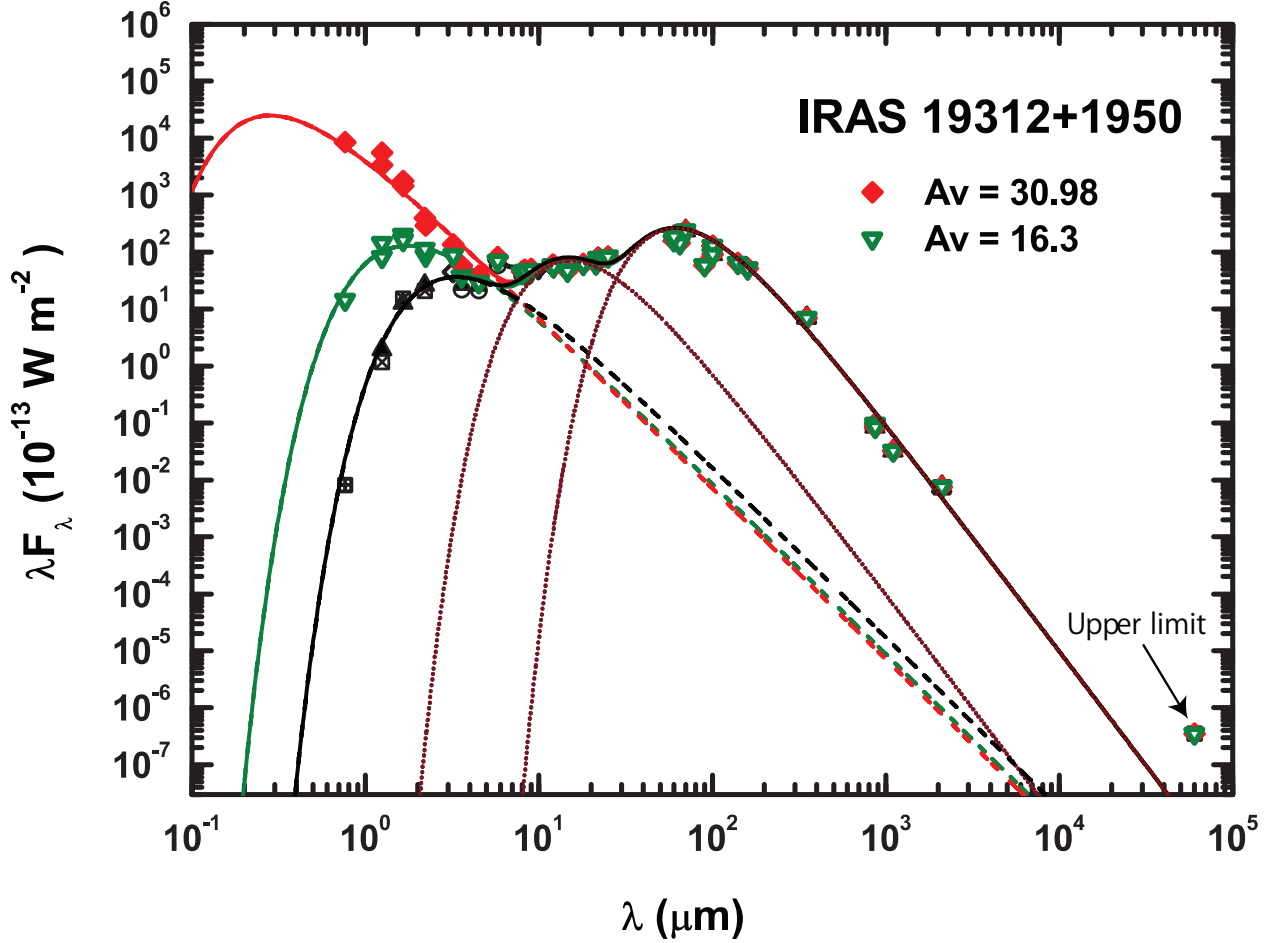


Fig. 7.— Spectral energy distribution (SED) diagram of I19312 with extinction corrections in the wavelength range from $0.1 \mu\text{m}$ to 10 cm . The crossed square, crossed diamonds, filled triangles, open diamonds, half-filled circles correspond respectively to the data of IPHAS i' -band photometry, J , H , and K near-infrared photometry, 2MASS, WISE, and Spitzer GLIMPSE survey (though, some of them may be unrecognizable due to overlapping with other symbols). The green open triangles and red filled diamonds respectively represent the photometric data corrected using the extinction values of $A(V) = 16.3$ and $A(V) = 30.98$. The black body curves are fitted to the emission from the photosphere (red, green, black lines) and two dust components (brown lines). The red, green and black lines represent the difference of the interstellar extinction corrections: i.e., $A(V) = 30.98$ (red), $A(V) = 16.3$ (green), and $A(V) = 0$ (black).